

# High resolution energy dispersive spectroscopy mapping of planar defects in L1<sub>2</sub>-containing Co-base superalloys

Titus, Michael S.; Mottura, Alessandro; Viswanathan, G. Babu; Suzuki, Akane; Mills, Michael J.; Pollock, Tresa M.

DOI:

[10.1016/j.actamat.2015.01.050](https://doi.org/10.1016/j.actamat.2015.01.050)

License:

None: All rights reserved

*Document Version*

Peer reviewed version

*Citation for published version (Harvard):*

Titus, MS, Mottura, A, Viswanathan, GB, Suzuki, A, Mills, MJ & Pollock, TM 2015, 'High resolution energy dispersive spectroscopy mapping of planar defects in L1<sub>2</sub>-containing Co-base superalloys', *Acta Materialia*, vol. 89, pp. 423–437. <https://doi.org/10.1016/j.actamat.2015.01.050>

[Link to publication on Research at Birmingham portal](#)

## **Publisher Rights Statement:**

Eligibility for repository: Checked on 4/2/2016

## **General rights**

Unless a licence is specified above, all rights (including copyright and moral rights) in this document are retained by the authors and/or the copyright holders. The express permission of the copyright holder must be obtained for any use of this material other than for purposes permitted by law.

- Users may freely distribute the URL that is used to identify this publication.
- Users may download and/or print one copy of the publication from the University of Birmingham research portal for the purpose of private study or non-commercial research.
- User may use extracts from the document in line with the concept of 'fair dealing' under the Copyright, Designs and Patents Act 1988 (?)
- Users may not further distribute the material nor use it for the purposes of commercial gain.

Where a licence is displayed above, please note the terms and conditions of the licence govern your use of this document.

When citing, please reference the published version.

## **Take down policy**

While the University of Birmingham exercises care and attention in making items available there are rare occasions when an item has been uploaded in error or has been deemed to be commercially or otherwise sensitive.

If you believe that this is the case for this document, please contact [UBIRA@lists.bham.ac.uk](mailto:UBIRA@lists.bham.ac.uk) providing details and we will remove access to the work immediately and investigate.

# High Resolution Energy Dispersive Spectroscopy Mapping of Planar Defects in L1<sub>2</sub>-containing Co-base Superalloys

Michael S. Titus<sup>a,\*</sup>, Alessandro Mottura<sup>b</sup>, G. Babu Viswanathan<sup>c</sup>, Akane Suzuki<sup>d</sup>, Michael J. Mills<sup>c</sup>, Tresa M. Pollock<sup>a</sup>

<sup>a</sup>Materials Department, University of California Santa Barbara, Santa Barbara, CA 93106-5050, USA

<sup>b</sup>Department of Metallurgy and Materials, University of Birmingham, Edgbaston, Birmingham B15 2TT, UK

<sup>c</sup>Center for Electron Microscopy Analysis, The Ohio State University, Columbus, OH 43210, USA

<sup>d</sup>GE Global Research, Niskayuna, NY 12309, USA

---

## Abstract

Local chemical fluctuations in the vicinity of superlattice intrinsic stacking faults (SISFs) have been observed via high resolution energy dispersive X-ray spectroscopy (EDS) mapping in new single crystal Co- and CoNi-base superalloys containing  $\gamma'$ -(L1<sub>2</sub>) precipitates. The SISFs were formed during high temperature tensile creep at 900°C. Chemical fluctuations were found to greatly influence the SISF energy, which was calculated from density functional theory in Co<sub>3</sub>(Al, Ta, W) compounds at 0 K. The local SISF structure was found to be comprised of four D0<sub>19</sub> (0001) planes that were enriched in W and Ta, as revealed by high resolution scanning transmission electron microscopy (HRSTEM) imaging and EDS mapping. The precipitates were determined to accommodate up to 22% of the plastic deformation accrued during an interrupted creep test to 0.6% creep strain. The driving forces for segregation are discussed, and new models for shearing of the ordered precipitates are proposed.

**Keywords:** Cobalt alloys; High temperature creep; Scanning transmission electron microscopy; Energy dispersive x-ray spectroscopy; Stacking faults

---

## 1. Introduction

Recently, the discovery of a  $\gamma'$ -(L1<sub>2</sub>) (ordered FCC) phase that is in equilibrium with a solid-solution  $\gamma$ -(A1) (FCC) phase has provided a pathway for the development of a new class of high temperature structural materials [1]. New alloys based on ternary Co-Al-W compositions have been shown to exhibit comparable and, in some cases, potentially superior single

crystal creep resistance at elevated temperatures, compared to Ni-base superalloys [2–6]. Due to their attractive creep properties, these alloys show potential for use as the structural components in high temperature engineering systems such as gas turbine engines. The new Co-base superalloys contain coherently-embedded  $\gamma'$  precipitates in the relatively soft and ductile  $\gamma$  matrix. As such, the alloys possess microstructures similar to Ni-base superalloys, with the distinction that the  $\gamma$ - $\gamma'$  misfit is generally positive in Co-base superalloys (i.e.  $a_{\gamma'} > a_{\gamma}$ ) [1–4, 7–10]. Other recent studies have shown that Co-base alloys are resistant to formation of single crystal casting defects, exhibit good polycrystalline creep strength, and possess comparable single crystal yield strength compared to Ni-base superalloys at elevated temperature [7, 11–15].

Analysis of high temperature ( $>850^{\circ}\text{C}$ ) creep-deformed Co-base alloys via transmission electron microscopy (TEM) has revealed a propensity for planar defect formation in the  $\gamma'$  phase [16, 17]. The planar defects, which have been identified as antiphase boundaries (APBs) and superlattice intrinsic stacking faults (SISFs), are formed as a result of dislocation shearing processes in the  $\gamma'$  precipitates. The creep-induced stacking faults in Co-base alloys typically span across one precipitate, are present on all four octahedral planes, and tend to form at elevated temperatures, beyond  $850^{\circ}\text{C}$  [5, 17]. These characteristics of fault formation differ from single crystal Ni-base alloys where the faults form at lower temperatures and higher stresses, span across multiple contiguous precipitates, and are typically observed on one or two octahedral planes [18–21].

Recently, creep-induced segregation along SISFs in Ni-base superalloys was observed by Viswanathan et al. [22]. Various  $\gamma$ -forming elements (Co, Cr, and Mo) were observed to segregate to the SISFs, with depletion of  $\gamma'$ -forming elements (Ni and Al). The authors considered Suzuki segregation as an explanation for the segregation behavior observed, though at present little is known about how Suzuki segregation affects the creep response of Ni-base superalloys.

In this paper, we analyze planar defects in Co- and CoNi-base superalloys in an edge-on configuration so that the stacking sequence may be analyzed. Furthermore, any chemical fluctuations near the planar defects may be observed using Z-contrast scanning transmission electron microscopy high-angle annular dark field (STEM HAADF) imaging and high reso-

lution energy dispersive X-ray spectroscopy (EDS) mapping. Analyses of the planar defects reveal that the structure of the stacking faults exhibit local hexagonal close-pack (HCP) stacking in addition to solute redistribution. The implications for creep strength and  $\gamma'$  shearing resistance due to chemical fluctuations in the vicinity of the faults are discussed.

## 2. Experimental Procedures

Four alloy compositions were investigated and the compositions are given in Table 1. The 2Ta, CrTa, and 6Ti alloys were directionally solidified via the Bridgman process, and the CoNi-C alloy was cast via the Liquid Metal Cooling process [11, 23, 24]. The single crystal bars were cast using withdrawal rates similar to those used for Ni-base superalloys [23, 25]. The single crystal bars, measuring approximately 15.2 cm in length, were approximately oriented in the [001] crystallographic direction. The bars were subsequently heat treated following the schedules given in Table 1. The heat treatment schedules allowed for initial solutioning of the  $\gamma'$  precipitates and subsequent aging at a lower temperature.

Single crystal button-head creep specimens measuring 7.6 cm in length were machined with a 3 mm-diameter gage section. All specimens were crept at 900°C under vacuum and at varying constant initial stresses, Table 2. The stress levels were chosen in order to obtain minimum creep rates in the vicinity of  $10^{-8} \text{ s}^{-1}$ . All creep tests were interrupted at approximately 0.6% or 2.0% creep strain and were subsequently investigated by conventional TEM.

Electron-transparent TEM foils were obtained by (1) sectioning the 3 mm-diameter gage section via electro-discharge machining, (2) mechanically grinding to approximately 100  $\mu\text{m}$  in thickness, and (3) electropolishing using an electrolytic solution of 92.5% methanol - 7.5% perchloric acid (by volume) at approximately -40°C, 16–20 V, and 24–30 mA. Conventional (parallel beam) TEM analysis was performed with a FEI T20 microscope equipped with a dual-axis large-angle tilt stage.

Because the specimens were ferromagnetic at room temperature, a FEI Helios Nanolab 600 FIB/SEM was used to machine approximately 100 nm-thick TEM lamellae for high resolution STEM imaging and EDS mapping. The TEM lamallae were extracted such that the [011] zone axis was approximately parallel to the sample normals. The TEM lamellae

were placed on a Mo grid using an Omniprobe W needle. Final thinning and cleaning of the approximately 10  $\mu\text{m}$ -wide lamellae was achieved by using a 1 keV FIB and 500 keV Ar ion beam using a Fischione NanoMill TEM specimen preparation system.

80 High resolution STEM imaging and EDS mapping at 300 keV were carried out using a Titan3™ G2 60-300 equipped with a monochromator for controlling probe current, and Super-X lens incorporating the Bruker ChemiSTEM system. The ChemiSTEM system uses four silicon drift detectors that are located radially around the objective pole piece and specimen stage for optimal collection efficiency. This system is described in further detail in  
85 Ref. [26–28].

Atomic resolution STEM imaging was obtained at a camera length of 91 mm in HAADF mode using a probe current of about 170 pA and convergence angle of 10.4 mrad. The probe size was specified to be 1.3 Å under optimal conditions, and Fourier transforms of the atomic resolution images indicated that a spatial resolution of 1.8 Å was achieved. The  
90 probe current was increased to 300 – 600 pA during EDS mapping in order to increase X-ray counts and decrease collection times. The spherical aberration correction coefficient,  $C_s$ , was specified to be 1.2 mm. The EDS maps were collected over an approximately 11 x 23 nm<sup>2</sup> area and analyzed using the Bruker ESPRIT software that incorporated drift correction during collection periods.

95 Vertically-integrated line scans were obtained across the faults as a means to increase the signal-to-noise ratio in the EDS data. The line scans were quantified using Cliff-Lorimer analysis and  $K\alpha$  lines for Co, Ni, Al, Cr, and Ti, and  $L\alpha$  lines for W and Ta. Due to spurious Cu and Mo signal originating from the specimen holder and/or instrument lenses, deconvolution was incorporated and the Cu and Mo compositions were fixed to 0 at.% for  
100 the quantification. Automated background subtraction was used on the Bremsstrahlung background noise in the EDS spectra.

### 3. Results

A conventional TEM (CTEM) centered dark field image of the 2Ta alloy crept at 900°C and 345 MPa for 88 hours to 0.6% creep strain with a minimum creep rate of  $6.7 \times 10^{-9} \text{ s}^{-1}$   
105 is shown in Figure 1a. In this dark field micrograph using  $\mathbf{g}=(200)$  and  $\mathbf{s}=0$  conditions,

numerous stacking faults are observed (ribbon/fringe-like contrast) in the  $\gamma'$  precipitates. The faults are inclined in the 2D projection of the 3D foil because the beam direction is nearly parallel to the  $[001]$  direction, which is parallel to the applied tensile load. The faults were determined to be of either intrinsic or extrinsic character [29–31]. Superlattice intrinsic  
110 stacking faults (SISFs) contain a bright fringe on the side of the fault toward which the  $\mathbf{g}$ -vector points, as shown by the white arrow labeled “SISF” in Figure 1a. Superlattice extrinsic stacking faults (SESFs) contain the bright fringe on the other side of the fault, relative to the  $\mathbf{g}$ -vector, as shown by the white arrow labeled “SESF” in Figure 1a. In this micrograph, the faults were observed on all four octahedral  $\{111\}$  planes.

115 A CTEM bright field image of the 2Ta alloy crept to 2.0% is shown in Figure 1b. Due to the large number of overlapping SISFs and SESFs in the precipitates, the precipitates appear dark when viewed from the  $[001]$  direction. The number of faults thus increases with increasing creep strain from 0.6% to 2.0%, as can be seen when comparing Figures 1a and 1b. The 2Ta sample, whose normal was parallel to the  $[011]$  direction, revealed two  $\{111\}$  planes  
120 edge-on, as shown in Figure 1c. The two  $\{111\}$  planes are about  $114^\circ$  apart. The faults on these  $\{111\}$  planes now appear as thin black lines spanning across the precipitates as shown by the dotted arrows in Figure 1c. High resolution HAADF STEM was employed for this and other TEM lamellae to investigate local stacking sequences and any segregation/depletion of elements across the fault plane.

### 125 3.1. High Resolution STEM Imaging

High resolution HAADF STEM imaging revealed enhanced contrast near the SISFs and SESFs as shown in micrographs from the 2Ta alloy in Figures 2a and 2d. The enhanced contrast suggests enrichment of heavy elements, for this alloy W and Ta, to the SISF or the depletion of relatively lighter elements such as Al and Co. Thirty-four other SISFs and SESFs  
130 were observed to exhibit similar image contrast within five adjacent precipitates. Typical “ABCABC” FCC stacking was observed along the  $[111]$  direction outside both faults, but local HCP (“CACA”) stacking was observed in the SISF, as shown in Figures 2a and 2b. The stacking sequence in the SESF was observed to be of “CACBC” stacking. The local structures of SISFs and SESFs have been proposed to consist of four  $D0_{19}$  (0001) layers and

seven (0001)  $\text{D}_{0_{24}}$  layers, respectively [32]. The HAADF STEM images in Figures 2a and 2d clearly indicate that ordering is maintained in the stacking faults, and the stacking sequences previously mentioned confirm that the local structure for the SISF and SESF are of  $\text{D}_{0_{19}}$  and  $\text{D}_{0_{24}}$  structure, respectively. An overview of relevant crystal structures and phases are given in Table 3.

Vertically-integrated line profile intensity plots across the SISF and SESF are shown in Figures 2c and 2f. The line profiles quantitatively reveal enhanced intensity along the SISF and SESF. The SISF profile exhibits enhanced contrast across the four  $\{111\}$  planes that comprise the fault and are associated with the “CACA” stacking in Figure 2b. Similarly, the SESF profile shows primary enhanced contrast across five  $\{111\}$  planes, with lower/secondary intensity contained in the two bordering  $\{111\}$  planes. The largest/primary intensity in the SESF is located in the “CACBC” planes in the SESF (Figure 2e), and the lower/secondary intensity is located on the adjacent B and A planes. The vertically-integrated line profiles additionally revealed no change in  $\{111\}$  plane spacings near the faults.

The width of the enhanced intensity region in the SISF was found to be 8.6 Å by measuring the distance between the troughs bracketing the “CACA” planes in the HAADF intensity line scan in Figure 2c. Similarly, the greatest/primary intensity (over the “CACBC” planes) was measured to be 9.9 Å in the SESF from Figure 2f. When the two bordering planes were incorporated, the enhanced contrast width increased to 14.2 Å.

### 3.2. Chemical Fluctuations near SISFs

EDS mapping was conducted to verify chemical fluctuations of various elements to and from the SISFs, as shown in Figure 3. Segregation of W and Ta to the SISF was observed, as indicated by the faint increase in intensity in the W and Ta EDS maps shown in Figure 3d and 3e. Simultaneously, depletion of Co and Al was observed in the SISF as shown in Figures 3b and 3c. All investigated faults exhibited the same chemical fluctuation behavior, and similar trends were observed for the other three alloys investigated here.

Vertically-integrated EDS line scans across the SISFs in all alloys are shown in Figure 4. The line scans show the percent change in composition compared to the average  $\gamma'$  composition. The individual elements are offset from each other by 30% for clarity. The

local concentration of alloy elements, except for Ti, was observed to fluctuate in the vicinity  
of the SISFs. Cobalt was observed to always deplete from the SISF for all three Co-base  
alloys (2Ta, CrTa, and 6Ti), as shown in Figure 4. However, Co was observed to segregate  
to the SISF in the CoNi-C alloy, presumably due to the significant Ni content. Aluminum  
was observed to deplete away from the SISF in all alloys, whereas Ta and W were observed  
to always segregate to the SISF. The Ti concentration did not change near the SISF. The  
Cr content decreased near the SISF in the CrTa alloy, but the Cr content increased near the  
SISF in the CoNi-C alloy. An overview of all chemical fluctuation trends is given in Table 4.

The chemical fluctuation widths of all four elements in the 2Ta alloy SISF was determined  
to be about 12.2 Å. This width was measured with reference to the two points surrounding  
the SISF where the composition returns to the surrounding L1<sub>2</sub> composition, Figure 4a.  
This chemical fluctuation width is about 3.6 Å, or 41%, larger than enhanced intensity  
width determined from the HAADF intensity profile in Figure 2c. Differences in chemical  
fluctuation widths indicate that electron channeling may be influencing the EDS signal or  
that specimen drift slightly smeared the EDS signal.

#### 4. The Driving Forces for Chemical Fluctuations and Segregation

While chemical fluctuations near stacking faults and other crystal defects have been  
widely hypothesized to govern a number of important aspects of mechanical behavior in  
metals, only recently has the instrumentation advanced to the level where the driving forces  
responsible for these chemical fluctuations can be studied. The present Co-base alloys provide  
a unique opportunity to investigate the driving forces responsible for chemical fluctuations,  
as the  $\gamma'$ -(L1<sub>2</sub>) phase can be in equilibrium with the nearby Co<sub>3</sub>W-(D0<sub>19</sub>) phase field. As  
mentioned previously, the local structure of the creep-induced SISFs observed in the Co-base  
alloys is comprised of the D0<sub>19</sub> structure, and thus direct comparisons can be made between  
the equilibrium Co<sub>3</sub>W-(D0<sub>19</sub>) phase and shear-induced SISF-(D0<sub>19</sub>) structure. An overview  
of experimental observations of chemical fluctuations in the vicinity of various planar defects  
is first presented, followed by first-principles analyses that elucidate the effects of chemical  
fluctuations on the SISF energy. Suzuki segregation along the SISFs and its effect on the  
 $\gamma'$  shearing mechanisms is then considered. Due to the significant chemical fluctuations



observed near SISFs, the effect of solute atmospheres on the shearing dislocations is also considered. Finally, the implications to the experimental creep strain rates are made.

195 The interaction of solute with stacking faults was first considered by Suzuki in 1952 [33]. Subsequent atom probe investigations 33 years after Suzuki’s original work provided some evidence for segregation of solute species to stacking faults [34], but only recently have TEM investigations yielded semi-quantitative results [35–38]. Enhanced Z-contrast along stacking faults and coherent twin boundaries in Mg alloys have been observed [38, 39], and indications  
200 of segregation occurring at stacking faults via EDS line scans have been reported by Han et al. and Mendis et al. [35, 36] in NiCo-base and Cu-Si alloys, respectively. However, Suzuki segregation has only been considered in solid-solution alloys and not ordered, intermetallic compounds.

Molybdenum, Al, Nb, and Ti were occasionally observed to segregate to stacking faults  
205 and slip bands after deformation at 630°C in an A3-containing NiCo-base superalloy investigated by Han et al. [35]. The driving force for segregation was attributed to the lowering of the stacking fault energy at elevated temperatures. Segregation was not observed at every stacking fault, and the researchers could not discern whether this was due to real differences or technique limitations. The experimental technique included the use of a FEI F20  
210 FEGTEM in the nanoprobe STEM mode with spot analyses acquired at about 1 nm intervals across the faults. The segregation analysis by Han et al. was ultimately limited by contamination due to long electron beam spot dwell times. However, with the emergence of new high efficiency X-ray detectors for TEM [26, 40], analysis may be conducted with counting statistics one to two orders of magnitude greater than in previous studies, which  
215 leads to a significantly increased signal-to-noise ratio.

High-resolution HAADF STEM experiments in a Ni-base superalloy, CMSX-4, have recently revealed enhanced atomic number (Z) contrast near creep-induced planar defects at 750°C and 750 MPa [41]. The authors attributed the enhanced contrast and periodic contrast to complex reordering or “atomic shuffles” which alter the initial planar defects -  
220 for example, from an antiphase boundary and complex intrinsic stacking fault to a SISF. Recently, chemical fluctuations along SISFs that formed during creep at 750°C in the  $\gamma'$  phase in Ni-base superalloys CMSX-4 and ME3 were observed by Viswanathan et al. [22]

using the same ChemiSTEM system as outlined in Section 2. In the CMSX-4 alloy, Co and Cr were enriched at the SISF while Al and Ni were depleted. This result is in contrast to the results from Han et al. [35], but is similar to the chemical fluctuations observed in the CoNi-C alloy in the present study and phase field modeling of a NiCo-base superalloy [37]. Qualitative and semi-quantitative chemical analysis presented here and by Viswanathan et al. [22] clearly demonstrates that chemical fluctuations occur in the vicinity of SISFs in the  $\gamma'$  phase in these Co-, CoNi-, and Ni-base alloys during the high temperature creep process ( $T/T_m > 0.6$ ) where diffusion easily occurs. However, the driving force and mechanisms responsible for these chemical fluctuations remain to be addressed. The effects of fault formation and chemical fluctuations at SISFs on the creep deformation process have not yet been investigated in any detail.

Insights into the mechanism and driving force for solute redistribution at faults may be inferred by considering the “direction” of compositional change from the equilibrium  $\gamma'$  composition compared to the local SISF composition. As Al is depleted from the SISF and W is enhanced for all Co- and CoNi-base alloys investigated here, the change in composition can roughly be characterized as trending toward the equilibrium  $\text{Co}_3\text{W}$ -(D0<sub>19</sub>) phase in the Co-Al-W ternary phase diagram, as shown by the red arrow in Figure 5. The D0<sub>19</sub> phase is relevant in this case as it is the local SISF structure resulting from a pure  $\frac{1}{3}\langle 112 \rangle$  shear event in the L1<sub>2</sub> structure [32]. The trends in chemical fluctuations at SISFs in both Co- and CoNi-base superalloys suggest that a lower energy configuration is achieved when the local D0<sub>19</sub> SISF structure is allowed, by local diffusional processes during high temperature creep, to reach a more stable composition, i.e.  $\text{Co}_3\text{W}$ -like in composition. First-principles calculations have thus been carried out to assess the SISF energy as a function of composition in the pseudo-ternary  $\text{Co}_3\text{Ta}$ - $\text{Co}_3\text{Al}$ - $\text{Co}_3\text{W}$  system.

#### 4.1. First-Principles Calculations

Obtaining SISF energies for a quaternary, ordered L1<sub>2</sub> phase (Co-Al-W-Ta), from first principles is not trivial with traditional supercell approaches. It is not yet possible, due to computational limitations, to emulate a random distribution of Al, W and Ta on the second sub-lattice of a supercell with high aspect ratio. In contrast, the axial next-nearest-

neighbour Ising (ANNNI) model [42], in conjunction with special quasi random structures (SQSs) [43], can be used to obtain reliable estimates of the SISF energy of the  $\gamma'$  phase with varying composition of Al, W and Ta on the second sub-lattice. This approach was followed, for example, to estimate the SISF energy of  $\text{Co}_3(\text{Al}_{0.5}\text{W}_{0.5})\text{-(L1}_2\text{)}$  in [44]. To explore the compositional space relevant to the present experimental observations, this procedure was extended by obtaining SQSs of the  $\text{L1}_2$  and  $\text{D0}_{19}$  crystal structures for several different compositions of the second sub-lattice. Specifically, multiple SQSs were constructed for  $\text{A}_3(\text{B}_{0.5}\text{C}_{0.5})$ ,  $\text{A}_3(\text{B}_{0.33}\text{C}_{0.66})$ ,  $\text{A}_3(\text{B}_{0.33}\text{C}_{0.33}\text{D}_{0.33})$  and  $\text{A}_3(\text{B}_{0.25}\text{C}_{0.25}\text{D}_{0.5})$  for both the  $\text{L1}_2$  and  $\text{D0}_{19}$  crystal structures. Further detail on the selected SQSs is provided in Appendix A. The total energies of these SQSs with different occupations of the B, C and D sites with Al, W and Ta were obtained using density functional theory (DFT) [45, 46] as implemented in the Vienna Ab-initio Simulation Package (VASP) [47, 48]. DFT was also used to obtain the total energies of  $\text{Co}_3\text{Al}$ ,  $\text{Co}_3\text{W}$  and  $\text{Co}_3\text{Ta}$  in the  $\text{L1}_2$  and  $\text{D0}_{19}$  crystal structures. All relevant simulation parameters are provided in Appendix A.

Once all total energies were obtained, the ANNNI model was then used to estimate SISF energies at discrete compositions of a hypothetical  $\gamma'$  phase extending across the  $\text{Co}_3\text{Ta-Co}_3\text{Al-Co}_3\text{W}$  pseudo-ternary (see Figure 6a). Unfortunately, obtaining finer-scale compositional data within the pseudo-ternary is not currently feasible since this would require the search of larger SQSs, which becomes computationally prohibitive. Nevertheless, the available data are enough to provide a clear picture of how SISF energy may change within the pseudo-ternary. It can be readily noticed that some compositions lead to a *negative* SISF energy (e.g.  $\text{Co}_3\text{Al}$ ,  $\text{Co}_3\text{W}$ ). This simply indicates that the total energy of the  $\text{D0}_{19}$  structure at that composition is lower (i.e. more stable) than the total energy of the  $\text{L1}_2$  structure for the same composition. Examining the  $\text{Co}_3\text{Al-Co}_3\text{W}$  pseudo-binary, it can be seen that the SISF energy sharply increases and reaches a maximum at  $\text{Co}_3(\text{Al}_{.33}\text{W}_{.66})$ , as shown in Figure 6a. With the addition of Ta, the SISF energy can be observed to increase and reach a maximum for  $\text{Co}_3(\text{Al}_{.33}\text{W}_{.33}\text{Ta}_{.33})$ .

Assuming that the SISF energy changes smoothly with composition across the  $\text{Co}_3\text{Al-Co}_3\text{W-Co}_3\text{Ta}$  pseudo-ternary, and that local atomic arrangements at the fault have a negligible effect on the SISF energy, the first-principles data can be fit with a  $n$ -dimensional Gaussian

process [49, 50]. This serves to highlight trends across the pseudo-ternary and to interpolate and quantify values of SISF energy for finer compositional variations. The fitting process interpolates between calculated SISF energies, and the confidence interval increases as the process moves further away from the computed data. The calculated SISF energy across the full pseudo-ternary is presented in Figure 6b. In accordance with previously reported calculations [44], it can be seen that the addition of Ta to a  $\text{Co}_3(\text{Al}, \text{W})$  compound can result in an increase in SISF energy. An increase in SISF energy has been hypothesized to increase creep resistance in Co-base alloys by increasing the resistance to dislocation shearing of the  $\gamma'$  phase due to a larger energy barrier of creating an extended SISF [4, 44].

In order to get a sense of the reduction in SISF energy due to chemical fluctuations, two structures from Figure 6a were chosen such that their change in composition was similar to the experimentally-observed trends. The  $\text{Co}_3(\text{Al}_{0.25}, \text{W}_{0.5}, \text{Ta}_{0.25})$  and  $\text{Co}_3(\text{W}_{0.66}, \text{Ta}_{0.33})$  compounds exhibited SISF energies of 99 and  $-98 \text{ mJ/m}^2$ , respectively. This corresponds to approximately a  $30 \text{ mJ/m}^2$  reduction in SISF energy per 1 at.% change in Al content (exchanging for W and Ta). Therefore, even small chemical fluctuations in the vicinity of the SISF can significantly influence the SISF energy.

#### 4.2. Suzuki Segregation

Segregation of solute to stacking faults has been proposed as a mechanism for locking dislocations and increasing yield strength with increasing solute content in Cu-Ni and Au-Ag binary alloys. This segregation mechanism has been termed *Suzuki Segregation* [33, 51, 52] and has been only applied to solid-solution alloys. Further theoretical work summarized by Hirth provided a framework in which the Suzuki breakaway stress for dislocations could be predicted from information on the dependence of stacking fault energy with composition in a [53]. It is clear that theoretically calculated stacking fault energies of compounds must include solute effects, which enables more realistic predictions of stacking fault energies in alloys under conditions where significant diffusion occurs.

The DFT calculations presented in Section 4.1 reveal that the SISF energy is significantly influenced by the local composition at the stacking fault. Assuming that chemical fluctuations near the SISFs decrease the stacking fault energy, scenarios in which dislocation

shearing may be accommodated by segregation can be envisaged, as shown in Figure 7.

A SISF may form in the  $\gamma'$  precipitates via the reaction between two  $\gamma$  matrix dislocations [14]. Consider two  $\frac{1}{2}\langle 110 \rangle$  dislocations interacting in the  $\gamma$  matrix such that two Shockley superpartial dislocations are created according to

$$\frac{1}{2}[101] + \frac{1}{2}[011] \rightarrow \frac{1}{3}[112] + SISF + \frac{1}{6}[112] \quad (1)$$

315 where *SISF* refers to the superlattice intrinsic stacking fault created inside the  $\gamma'$  precipitate after the leading  $\frac{1}{3}[112]$  dislocation enters the precipitate. In this configuration, the common slip plane is  $(11\bar{1})$  and the leading  $\frac{1}{3}[112]$  dislocation has a line direction approximately parallel to the  $[1\bar{1}0]$  direction. Hence, both dislocations are approximated to be of edge character with their Burgers vectors parallel to each other. The resolved shear stress,  $\tau$ , vs. 320 dislocation separation distance,  $r$ , of this configuration may be determined by:

$$\tau = \frac{\gamma}{b} - \frac{\mu a^2}{6\pi b r (1 - \nu)} \quad (2)$$

where  $\gamma$  is the SISF energy,  $\mu$  is the shear modulus,  $a$  is the  $\gamma'$  phase lattice parameter,  $b$  is the magnitude of the leading  $\frac{1}{3}[112]$  dislocation, and  $\nu$  is Poisson's ratio. This equation is only valid for configurations where a trailing partial dislocation is pinned at the  $\gamma$ - $\gamma'$  interface behind the leading shearing superpartial dislocation, as shown in Figures 7a-c.

325 Following the analysis from Hirth [53], the breakaway stress for the leading Shockley superpartial dislocation may be estimated by considering the SISF energies in the segregated and unsegregated state. We propose that the sequence of dislocation shearing includes: (1) a reaction occurring at the  $\gamma$ - $\gamma'$  interface according to Equation 1, (2) penetration of the leading  $\frac{1}{3}[112]$  dislocation into the  $\gamma'$  phase such that, under zero applied stress, an equilibrium 330 separation with a segregated SISF would be achieved, as shown in Figure 7a, (3a) the leading dislocation begins to glide after a critical stress, leaving behind an unsegregated SISF, as shown in Figure 7b and 7c, or (3b) the leading dislocation begins to glide immediately, leaving behind a segregated SISF.

The sequence of dislocation escape is shown schematically in Figure 7d in a plot of  $\tau$  335 vs.  $r$  for an unsegregated SISF energy of  $\gamma_0$  and two segregated SISF energies,  $\gamma_{s1}$  and  $\gamma_{s2}$ ,

given by  $\gamma_0 > \gamma_{s1} > \gamma_{s2}$ . The equilibrium separations,  $r_{e1}$  and  $r_{e2}$ , shown in Figure 7d may be determined from conventional dislocation analysis for segregated SISF energies of  $\gamma_{s1}$  and  $\gamma_{s2}$ , respectively. The initial dislocation configuration shown in Figure 7a is locked until a stress of  $(\gamma_0 - \gamma_s)/b$  is achieved, where  $\gamma_s$  represents either segregated SISF energies ( $\gamma_{s1}$  and  $\gamma_{s2}$ ), per Hirth's analysis [53].

When the stress reaches the critical stress from Hirth's analysis, the dislocation will begin to glide away from the trailing partial dislocation according to Equation 2. Once a stress of  $\gamma_0/b$  is achieved, the dislocation will completely escape from the trailing partial dislocation and glide until it reaches an obstacle or region of lower stress.

If chemical fluctuations at the stacking fault occur dynamically during the shearing process, then the breakaway stress will be even further reduced to simply  $\tau_{RSS} = \gamma_s/b$ , as previously mentioned. For SISF energies of 100, 75, and 25 mJ/m<sup>2</sup>, the critical resolved shear stresses for dislocation breakaway are 341, 256, and 85 MPa, respectively. Under a uniaxial tensile stress of 345 MPa (the experimental conditions studied here), the resolved shear stress for the  $\langle 112 \rangle \{11\bar{1}\}$  slip system is 162 MPa. This would imply that a SISF energy of about 47 mJ/m<sup>2</sup> is required to allow shearing of the  $\gamma'$  phase, assuming that misfit stresses are negligible. As such, the SISF energy must only be reduced by an amount necessary to accommodate shearing of the  $\gamma'$  phase, and the local SISF composition will not need to shift completely to the Co<sub>3</sub>W composition to accomplish this reduction in SISF energy. Therefore, if two  $\gamma$  matrix dislocations of type  $\frac{1}{2}\langle 110 \rangle$  are able to react and form  $\frac{1}{3}[112]$  dislocations in the early stages of creep, shearing of the  $\gamma'$ -precipitates at low creep strains (e.g. 0.6%) is possible for segregated SISF energies that are near  $\gamma_s = \tau b$ , where  $\tau$  is the resolved shear stress, arising from the uniaxial creep stress, on a  $\frac{1}{3}[112]$  dislocation.

From the previous analysis, it is clear that a reduction in the SISF energy would significantly impact the critical resolved shear stress for  $\gamma'$  shearing due to the Shockley superpartial dislocations. And, as mentioned previously, the compositional fluctuations in the vicinity of the fault would serve to shift the local composition toward a thermodynamically lower energy state, i.e. toward equilibrium D0<sub>19</sub> composition. Thus it is worth viewing this compositional fluctuation as arising from a displacive-diffusive phase transformation.

### 4.3. Displacive-Diffusive $L1_2 \rightarrow D0_{19}/D0_{24}$ Phase Transformation

Displacive and displacive-diffusive phase transformations involving  $A1 \rightarrow A3$ ,  $A1 \rightarrow D0_{19}$ ,  $L1_2 \rightarrow D0_{19}$ , and  $L1_0 \rightarrow D0_{19}$  reactions have been the subject of several detailed investigations [54–57]. The  $A1 \rightarrow A3$  phase transformation simply involves the long-range separation of  $\frac{1}{6}\langle 112 \rangle$  Shockley partial dislocations that are connected by a stacking fault of local  $A3$  structure. Ledge formation via dislocation nucleation on adjacent  $\{111\}$  planes accommodates lateral growth of the original stacking fault into an  $A3$  precipitate plate. Continuous precipitation of the  $D0_{19}$  phase, then, requires an additional compositional shift at the stacking faults, and final shuffling enables an ordered  $D0_{19}$  (HCP) structure to form [57]. As such, if a continuous precipitation phase transformation is to be considered as a driving force for SISF formation, the details of the combined displacive and diffusive transformation must be examined.

The local structure resulting from the glide of  $\frac{1}{3}\langle 112 \rangle\{111\}$  Shockley superpartial dislocations across the  $\gamma'-(L1_2)$  phase results in the formation of a SISF, which is equivalent to four (0001) planes of the  $D0_{19}$  structure. The  $D0_{19}$  structure exhibits a  $\langle 11\bar{2}0 \rangle(0001) \parallel \langle 110 \rangle\{111\}$  orientation relationship with the  $L1_2$  phase [57]. This orientation relationship maintains coherency between the  $L1_2$  and  $D0_{19}$  phases, at least for a single fault as in Figure 2a, and also maintains the correct stoichiometry for the  $L1_2$  phase on  $\{111\}$  planes. However, as the structure in the SISF is locally  $D0_{19}$ , its composition is Al- and Co-rich when compared to the nearby  $Co_3W$  field shown in Figure 5. In this scenario there is a driving force for solute redistribution to occur such that the local  $D0_{19}$  achieves a more stable chemical composition, as mentioned previously. Similarly, superlattice extrinsic stacking fault formation has been proposed to include a second  $\frac{1}{3}\langle 112 \rangle\{111\}$  Shockley superpartial dislocation gliding on a  $\{111\}$  plane adjacent to a pre-existing SISF [58, 59]. During SESF formation, the stoichiometry on the  $\{111\}_{L1_2}$  planes is maintained, but the local structure is now  $D0_{24}$ .

If a displacive-diffusive phase transformation occurs, then diffusion must occur as the dislocation shears the  $\gamma'$  precipitate. This may indicate that a Cottrell atmosphere is present near the shearing dislocation. As such, the velocity,  $v$ , of a dislocation in the presence of a

solute atmosphere may be estimated as [60]

$$v = \frac{(\tau b) D k T}{2.1 c_0 \beta^2} \quad (3)$$

where  $D$  is the interdiffusion constant,  $k$  is the Boltzmann constant,  $T$  is the temperature,  $c_0$  is the solute concentration,  $\beta$  is related to the interaction energy between the solute and dislocation, and the factor 2.1 arises from the size of the solute atmosphere and core cutoff distance [60, 61]. Taking  $D = 5 \times 10^{-18} \text{ m}^2/\text{s}$  (extrapolated interdiffusion coefficient in  $\gamma$ -(Co,W) at 900°C [62]),  $T = 1173 \text{ K}$ ,  $c_0 = 4 \times 10^{27} \text{ m}^{-3}$  (or 5at.%, estimated from the change in composition from  $\gamma'$  to  $\text{Co}_3\text{W}$ ),  $\beta = 1.6 \times 10^{-29} \text{ Nm}^2$ , and  $\tau b = (345 \text{ MPa} \times 0.471)(0.293 \text{ nm}) = 47 \text{ mN/m}$ , the dislocation velocity is determined to be  $2 \times 10^{-9} \text{ m/s}$ .

A shearing dislocation velocity of  $2 \times 10^{-9} \text{ m/s}$  would correspond to an active shearing dislocation density of about  $4 \times 10^{10} \text{ m}^{-2}$  assuming that the strain rate is governed solely by the active shearing dislocations. The active dislocation density,  $\rho$ , is calculated from the Orowan equation

$$\rho = \frac{2\dot{\epsilon}}{bv} \quad (4)$$

where  $\dot{\epsilon}$  is the minimum creep rate ( $\sim 10^{-8} \text{ s}^{-1}$ ). A dislocation density of  $4 \times 10^{10} \text{ m}^{-2}$  is about one to two orders of magnitude lower than other high temperature creep investigations of Ni-base alloys [63, 64]. Thus it is reasonable to assume that a significant fraction of the creep strain rate is governed by relatively slow-moving Shockley superpartial dislocations, which create SISFs in their wake during the shearing process.

In order to estimate the length scales over which diffusion may realistically take place in these alloys, a plot of diffusion length,  $x$ , vs. time is shown for three different diffusion coefficients following  $x = \sqrt{Dt}$ , as shown in Figure 8. Diffusion lengths of just 4 nm are possible within 20 s even for a diffusion coefficients of  $10^{-18} \text{ m}^2/\text{s}$ . Therefore, it appears that diffusion is possible during the displacive part of the transformation, which is rate controlled by the decomposition events at the  $\gamma$ - $\gamma'$  interface, and diffusion in the  $\gamma'$  phase could be the rate limiting step during shearing of the precipitates.

Additionally, if segregation is allowed to occur during the shearing process, the formation



of a  $D0_{19}$  plate-like structure may be akin to a Widmanstätten morphology arising from a  $L1_2 \rightarrow D0_{19}$  phase transformation, as has been observed by Carvalho et al. for  $A1 \rightarrow A3 \rightarrow D0_{19}$  [57]. Widmanstätten morphologies can occur in cubic matrices where the cubic symmetry allows for four possible HCP habit planes [65]. This morphology was observed in the 2Ta and CrTa alloys crept to rupture [4]. The formation of SISFs in the  $\gamma'$  precipitates may also serve as nucleation sites for  $Co_3W$  laths to form, and may explain the prevalence of SISFs and  $Co_3W$  laths observed in the 2Ta alloy as compared to the other Co-base alloys mentioned in Refs. [4, 17] with similar  $\gamma'$  volume fraction, morphology, and size.

The mechanism for local chemical fluctuations across the SISF could benefit from further diffusion investigations. Viswanathan et al. [22] proposed three mechanisms for diffusion of solute to/away from the SISFs: (1) diffusion that occurs perpendicular to the fault, (2) diffusion that occurs along the fault (presumably to/from the  $\gamma$  matrix), and (3) diffusion along the leading partial dislocation (e.g. pipe diffusion). The analyses presented here do not confirm or discredit any of the previous three hypotheses directly, but the consistent HAADF image intensity along the faults suggests that diffusion parallel to the fault plane did not occur in these alloys. Additionally, using core diffusion parameters for a Ni-base superalloy MAR-M200 ( $a_c D_{0c} = 10^{-26} \text{ m}^4/\text{s}$ ,  $Q_c = 170 \text{ kJ/mol}$ ) and an active shearing dislocation density ( $\rho = 2 \times 10^{10} \text{ m}^{-2}$ ), the dislocation core diffusion coefficient is determined to be  $D_c = 5 \times 10^{-24} \text{ m}^2/\text{s}$  [66]. This core diffusion coefficient would only correspond to a diffusion distance of about 1 nm over the course of a 90 h creep experiment at 900°C. Thus, it is reasonable to assume that the diffusion mechanism responsible for the chemical fluctuations near the SISFs is (1) diffusion that occurs perpendicular, or more generally, in the bulk of the  $\gamma'$  phase.

Due to limited experimental and theoretical analyses available for  $\gamma'$ -containing Co-base superalloys, a phase transformation mechanism for  $\gamma'$  shearing and SISF diffusion mechanisms cannot be verified presently. However, further investigations that determine and elucidate solute-defect interactions, interdiffusion and core diffusion coefficients, planar defect energies, dislocation core configurations, Gibbs free energy calculations, and strain rate dependencies on the segregation characteristics will provide sufficient evidence for the existence of these mechanisms.

## 5. Creep Deformation and Faulting of the $\gamma'$ Phase

The stacking faults in Co-base alloys additionally provide an opportunity to track the amount of deformation accommodated by the  $\gamma'$  precipitates, as the faults are essentially “tracers” of plastic deformation. It is well known in Ni-base alloys that long-range  $\gamma'$  shearing via planar fault formation accommodates a significant portion of plastic deformation during primary creep at low temperatures and high stresses (e.g. 750°C and 750 MPa) [21]. The total plastic deformation accommodated by a single planar fault ribbon is difficult to determine in these tests because the total slip distance of the superpartial dislocations is unknown. Furthermore, the  $\gamma'$  shearing mechanisms change at elevated temperatures ( $T > 850^\circ\text{C}$ ) in Ni-base alloys and shearing usually occurs via coupled  $\frac{1}{2}\langle 110 \rangle$  dislocations [63, 67, 68]. This mode of deformation does not leave behind any planar defects. Thus tracking the contribution of precipitate shearing and plastic deformation is again difficult. However, the stacking faults in Co-base alloys provide a marker of accumulated plastic deformation in the  $\gamma'$  precipitates because the faults typically do not extend beyond a single precipitate. The 2Ta alloy crept to 0.6% was thus investigated to determine the amount of plastic deformation accommodated by shearing of the  $\gamma'$  precipitates.

The calculated average shear strain,  $\bar{\gamma}$ , accommodated in the precipitates can be determined from the Orowan equation, such that

$$\bar{\gamma} = b_p \rho_{sp} \bar{x} \quad (5)$$

where  $\bar{x}$  is the average slip distance of the leading partial dislocation, and  $\rho_{sp}$  is the total Shockley superpartial dislocation density that has assisted to accommodate shearing of the  $\gamma'$  phase. Here the total shearing superpartial dislocation density was determined by

$$\rho_{sp} = \frac{n\bar{l}}{V} \quad (6)$$

where  $n$  is the average number of stacking faults per precipitate,  $\bar{l}$  is the average dislocation line length of the shearing Shockley superpartial dislocations, and  $V$  is the average precipitate volume in the 2Ta alloy crept to 0.6%. The average number of stacking faults per precipitate was determined to be 5.2. The average dislocation line length and precipitate volume,  $n$  and

$V$ , were calculated by  $\sqrt{2}L_0$  and  $L_0^3$ , respectively, where  $L_0$  is the average precipitate cube length of 422 nm. The total shearing superpartial dislocation density was calculated to be  $\rho_{sp} = 4.1 \times 10^{13} \text{ m}^{-2}$ .

475 The average width of the SISFs along the  $\langle 110 \rangle$  directions was determined to be 220 nm. Assuming that the average width of the SISFs is approximately equal to the average slip length along the  $\langle 112 \rangle$  directions<sup>1</sup>,  $\bar{x}$  is approximated to be 220 nm. Therefore, the average shear strain accommodated by  $\gamma'$  precipitates was found to be 0.26%. Finally, by invoking the Tresca criterion of  $\epsilon = \bar{\gamma}/2$ , the strain accommodated in the precipitates equates to 0.13%.  
 480 As such, shearing of the precipitates accommodates about 22% of the strain accumulated in the creep specimen in the early stages of creep.

The strain accommodated in the  $\gamma'$  precipitates will likely increase as the creep strain increases because the density of stacking faults increases significantly with increasing creep strain, as shown in Figures 1b and 1c. This may be further corroborated by analyzing the  
 485 dislocation networks formed in the  $\gamma$  channels and misfit dislocations deposited at the  $\gamma$ - $\gamma'$  interfaces. In the high temperature creep regime ( $T > 850^\circ\text{C}$ ), the dislocation networks have been observed to be very stable after their formation near the end of primary creep, and therefore are not expected to contribute significantly to the plastic deformation process at greater creep strains [68–70]. Instead, shearing of the  $\gamma'$  phase would likely contribute more  
 490 significantly after the dislocation networks are formed. Further investigations considering dislocation network configurations, dislocation spacings, and stacking fault densities could provide significantly improved understanding of the micromechanical deformation processes present during high temperature creep in these and other  $\gamma$ - $\gamma'$  superalloys.

## 6. Discussion

495 The chemical fluctuations observed across creep-induced superlattice intrinsic stacking faults (SISFs) in Co-base alloys are consistent with a significant decrease in SISF energy predicted from first-principles calculations. Chemical fluctuations near the SISF associated with stabilization of the  $\text{D0}_{19}$  phase occurred for all alloys investigated. In Co-base alloys, Co

---

<sup>1</sup>Initial investigations of  $\mathbf{n}=[111]$ -oriented TEM foils support this assumption.

and Al were always observed to deplete from the SISFs, and W and Ta were always observed  
 500 to segregate to the SISFs. Here we have considered the implications of Suzuki segregation  
 for shearing of ordered precipitates. This analysis combined with first-principles calculations  
 of SISF energies has indicated that a significant decrease in the SISF energy can greatly  
 reduce the stresses required for shearing, and that shearing of the  $\gamma'$  phase accommodates a  
 significant portion of plastic deformation even at low total creep strains.

505 Additionally, a comparison of TEM micrographs from specimens crept to 0.6% and 2.0%  
 creep strain indicates that the fault density increases significantly as the creep strain is  
 increased, as shown in Figures 1a and 1b. Assuming that  $\gamma$  matrix dislocation networks  
 remain very stable after primary creep, shearing of the  $\gamma'$  precipitates likely becomes the  
 most significant contributor to plastic deformation. Therefore, creep resistance would be  
 510 improved by reducing the driving force for shearing at elevated temperatures. Methods for  
 reducing the rate of shearing in Ni-base alloys at elevated temperatures include reducing  
 the climb velocity of dislocations present in both the  $\gamma$  and  $\gamma'$  phases [64]. Alloying of Pt-  
 group metals and Re in Ni-base alloys assist in reducing the interdiffusion coefficients and  
 climb velocity, and thus increase creep resistance at elevated temperatures [64]. However,  
 515 Co-base alloys are already significantly alloyed with W, which certainly reduces the rate of  
 interdiffusion [62]. Preliminary high temperature creep tests of polycrystalline Re-containing  
 CoNi-base alloys suggest that the creep resistance is not significantly affected by Re [71]; this  
 may be due to partitioning of solute to the phases being weaker compared to conventional  
 Ni-base alloys. New strategies for improving creep resistance must therefore be developed  
 520 for this class of L1<sub>2</sub>-containing superalloys.

One such strategy may be rationalized from considering the formation of  $\frac{1}{3}\langle 112 \rangle$  Shockley  
 superpartial dislocations, which require the proper sequence of reactions between  $\gamma$  matrix  
 dislocations. If the dislocation reactions may be prevented in the  $\gamma$  matrix, formation of  
 Shockley superpartial dislocations may be suppressed. This point is particularly relevant  
 525 when comparing deformation mechanisms observed in high temperature compression flow  
 stress tests in single phase  $\gamma'$ -Co<sub>3</sub>(Al,W) alloys and two phase  $\gamma$ - $\gamma'$  Co-Al-W-base alloys [14,  
 72]. Deformation of the  $\gamma'$  phase in single phase alloys near 900°C occurs via APB-coupled  
 $\frac{1}{2}\langle 101 \rangle$  superpartial dislocations [72]. The deformation mechanisms in two phase  $\gamma$ - $\gamma'$  Co-base

alloys differs from the previous mode in that SISF formation is prevalent via the dislocation  
 530 reaction in the  $\gamma$  matrix according to Equation 1 [14]. Therefore, microstructural control  
 through proper alloying and heat treatment schedules may provide barriers to dislocation  
 interactions. For example, to suppress dislocation interactions from adjacent or intersecting  
 $\gamma$  matrix channels, the  $\gamma'$  size could be increased so that the  $\gamma$  matrix dislocations require a  
 longer slip distance in order to reach adjacent or intersecting  $\gamma$  matrix channels. This would  
 535 decrease the Orowan stress ( $\tau = \mu b/d$ ) required for bowing, so the  $\gamma'$  volume fraction would  
 subsequently need to be increased as well. The  $\gamma'$  precipitate size may be increased via longer  
 aging heat treatment times; and increasing the  $\gamma'$  volume fraction can be accomplished via  
 alloying with  $\gamma'$ -forming elements such as Ta, Ti, and Nb.

The  $\gamma'$  size, morphology, and volume fraction all contribute to the relative creep resistance  
 540 of Co- and CoNi-base alloys [3, 4]. The  $\gamma'$  size was shown to potentially suppress SISF  
 formation, as the 6Ti alloy exhibited superior resistance to SISF formation compared to the  
 2Ta alloy of similar  $\gamma'$  volume fraction, morphology, and lattice misfit [17]. The 6Ti alloy  
 possesses a slightly larger  $\gamma'$  size in the as-aged and crept condition, compared to the 2Ta [17].  
 However, first-principles calculations have suggested that the SISF energy may be further  
 545 increased with Ti alloying additions, compared to Ta additions [44, 73]. Thus separating  
 the contributions of mechanisms for suppressing SISF formation based on microstructural  
 properties and SISF energies may be difficult to discern.

If the proper sequence of dislocation reactions takes place to form a Shockley super-  
 partial dislocation, increasing the SISF energy in the  $\gamma'$  phase would serve to increase the  
 550 resolved shear stress required for  $\gamma'$  shearing in accordance to Equation 2. The SISF energies  
 in the  $\text{Co}_3(\text{Al,W})$  compound may be increased via Ta and Ti additions [44, 73], and these  
 alloying additions possess the supplemental benefit of also increasing the  $\gamma'$  volume fraction,  
 as mentioned previously. However, if diffusion occurs during the shearing process of the  
 leading Shockley superpartial dislocation, SISF formation in the  $\gamma'$  phase likely occurs at  
 555 a much lower SISF energy than those calculated using DFT for stoichiometric compounds  
 [44]. This indicates that shearing involving SISF formation may only occur, for stresses less  
 than the yield strength, when significant diffusion processes are allowed to occur such that  
 the SISF energy is decreased through chemical fluctuations.

The driving forces associated with chemical fluctuations across the SISFs have been shown to be associated with a decrease in the calculated SISF energy and, possibly, with a thermodynamically-driven phase transformation. Fault formation could then be suppressed by alloying with elements that do not aid in the stabilization of a hexagonal (e.g.  $D0_{19}$  or  $D0_{24}$ ) phase and assist to increase the  $\gamma'$ -solvus and  $\gamma'$  volume fraction. Titanium is an example of such an alloying element because it exhibits no preferential segregation behavior near the SISF, nor is the  $D0_{19}/D0_{24}$ -(Co<sub>3</sub>Ti) phase stable [74, 75]. In fact, the  $\gamma'$ -(Co<sub>3</sub>Ti-L1<sub>2</sub>) phase is stable over a large temperature range in the Co-Ti binary system [74]. Tantalum and Nb, however, form a stable Co<sub>3</sub>(Ta,Nb)-(C36) compound, as shown recently by Zhou et al. [76]. For alloying elements that form hexagonal structures near the relevant L1<sub>2</sub> phase composition, it may be expected that the SISF energy can be easily reduced with slight enhancement of hexagonal-forming elements at the SISF. Thus relative stabilities between hexagonal and cubic structures may be used as an indicator for chemical fluctuation driving forces near SISFs of locally hexagonal-( $D0_{19}$ ) structure.

When the SISFs do form in the  $\gamma'$  phase at temperatures where diffusion is prevalent, the resulting structure is likely more resistant to subsequent shearing events because the local SISF composition differs from the surrounding  $\gamma'$  composition [77]. Recent TEM analysis of the Co-base alloys have revealed numerous interacting faults in the  $\gamma'$  phase [17], which suggests that the dislocations do not easily shear through preexisting SISFs and SESFs. Some interactions included faults that have intersected another fault, and other instances revealed the formation of a SESF after interactions between two SISFs. Assuming that the SISFs and SESFs form with a different chemical composition than the surrounding L1<sub>2</sub> structure, glide of shearing Shockley superpartial dislocations may be impeded by these thin SISF and SESF structures. However, this would only serve as a hardening mechanism, and would likely limit the recovery processes necessary to extend secondary creep life. Future modeling efforts may significantly enhance our understanding of SISF and SESF formation and the contribution of dislocation penetration within the  $\gamma'$  phase to the high temperature properties of this new class of alloys.

## 7. Conclusions

Analysis of chemical fluctuations near planar defects in Co-base alloys and first-principles modeling have provided insight into the nature and importance of high temperature creep shearing mechanisms, and new methods for increasing the  $\gamma'$  shearing resistance have been proposed. The following conclusions are drawn from this work:

1. Superlattice intrinsic and extrinsic stacking faults (SISFs and SESFs) in Co- and CoNi-base alloys formed in the  $\gamma'$  phase during high temperature creep deformation. The faults exhibited  $D0_{19}$  and  $D0_{24}$  structure, respectively.
2. Chemical fluctuations in the vicinity of SISFs were clearly detected by high resolution EDS mapping.
3. Ta and W were always observed to segregate to the SISFs, regardless of composition. Co and Al were always observed to deplete away from the SISFs for Co-base alloys, but Co segregated to and Ni depleted away from SISFs in CoNi-base alloys.
4. Chemical fluctuations across the SISFs were consistent with a decrease of the SISF energy, as calculated by first-principles methods.
5. The creep strain accommodated by shearing events in the  $\gamma'$  phase was determined to account for 22% of the accumulated 0.6% creep strain in the 2Ta alloy.
6. Alloying with transition metals that form stable cubic  $Co_3X$  phases is likely to improve the  $\gamma'$  shearing resistance as the driving force for chemical fluctuations across the stacking faults is reduced, compared to systems alloyed with elements that do not form stable cubic  $Co_3X$  phases.

**Acknowledgements:** The authors would like to acknowledge assistance from Drs. Robert Williams and Fan Yang (The Ohio State University) in STEM operation, and Dr. Frank Scheltens (The Ohio State University) for useful discussion regarding EDS data analysis. Profs. Anton Van der Ven and Carlos Levi (University of California, Santa Barbara) are also thanked for their productive discussions. This work was supported by the NSF DMR-REF Grant DMR 1233704. Prof. Mottura acknowledges the use of the BlueBEAR high performance computational facilities at the University of Birmingham. The MRL Shared Experimental Facilities are supported by the MRSEC Program of the NSF under Award

No. DMR 1121053; a member of the NSF-funded Materials Research Facilities Network (www.mrfln.org).

## References

- [1] J. Sato, T. Omori, K. Oikawa, I. Ohnuma, R. Kainuma, K. Ishida, Cobalt-base high-temperature alloys, Science (80-. ). 312 (2006) 90–91.
- [2] K. Tanaka, M. Ooshima, N. Tsuno, A. Sato, H. Inui, Creep deformation of single crystals of new CoAlW-based alloys with fcc/L12 two-phase microstructures, Philos. Mag. 92 (2012) 4011–4027.
- [3] M. S. Titus, A. Suzuki, T. M. Pollock, Creep and directional coarsening in single crystals of new  $\gamma/\gamma'$  cobalt-base alloys, Scr. Mater. 66 (2012) 574–577.
- [4] M. S. Titus, A. Suzuki, T. M. Pollock, High Temperature Creep of New L12-containing Cobalt-base Superalloys, in: Superalloys 2012, 2012, pp. 823–832.
- [5] F. Xue, H. Zhou, X. Chen, Q. Shi, H. Chang, M. Wang, X. Ding, Q. Feng, Creep behavior of a novel Co-Al-W-base single crystal alloy containing Ta and Ti at 982C, MATEC Web Conf. 14 (2014) 15002.
- [6] F. Xue, H. J. Zhou, Q. Feng, Improved High-Temperature Microstructural Stability and Creep Property of Novel Co-Base Single-Crystal Alloys Containing Ta and Ti, Jom (2014).
- [7] A. Bauer, S. Neumeier, F. Pyczak, R. Singer, M. Göken, Creep properties of different  $\gamma'$ -strengthened Co-base superalloys, Mater. Sci. Eng. A 550 (2012) 333–341.
- [8] F. Pyczak, a. Bauer, M. Göken, S. Neumeier, U. Lorenz, M. Oehring, N. Schell, a. Schreyer, a. Stark, F. Symanzik, Plastic deformation mechanisms in a crept L12 hardened Co-base superalloy, Mater. Sci. Eng. A 571 (2013) 13–18.
- [9] K. Tanaka, M. Ooshima, N. Okamoto, K. Kishida, H. Inui, Morphology change of gamma' precipitates in gamma/gamma' two-phase microstructure in Co-based superalloys by higher-order alloying, Mater. Res. Soc. Symp. Proc. 1295 (2011) 423–428.
- [10] H. Yan, V. Vorontsov, J. Coakley, N. G. Jones, H. J. Stone, D. Dye, Quaternary Alloying Effects and the Prospects for a New Generation of CoBase Superalloys, in: E. S. Huron, R. C. Reed, M. C. Hardy, M. J. Mills, R. E. Montero, P. D. Portella, J. Telesman (Eds.), Superalloys 2012, 112, 2012, pp. 705–714.
- [11] M. Tsunekane, A. Suzuki, T. M. Pollock, Single-crystal solidification of new CoAlW-base alloys, Intermetallics 19 (2011) 636–643.
- [12] A. Bauer, S. Neumeier, F. Pyczak, M. Göken, Microstructure and creep strength of different  $\gamma/\gamma'$ -strengthened Co-base superalloy variants, Scr. Mater. 63 (2010) 1197–1200.
- [13] A. Suzuki, G. C. DeNolf, T. M. Pollock, Flow stress anomalies in  $\gamma/\gamma'$  two-phase CoAlW-base alloys, Scr. Mater. 56 (2007) 385–388.
- [14] A. Suzuki, T. M. Pollock, High-temperature strength and deformation of  $\gamma/\gamma'$  two-phase CoAlW-base alloys, Acta Mater. 56 (2008) 1288–1297.
- [15] M. Knop, V. A. Vorontsov, M. C. Hardy, D. Dye, High-temperature  $\gamma$  (FCC)/  $\gamma$  (L1 2 ) Co-Al-W based superalloys, MATEC Web Conf. 14 (2014) 18003.
- [16] Y. M. Eggeler, M. S. Titus, A. Suzuki, T. M. Pollock, Creep deformation-induced antiphase boundaries in L12-containing single-crystal cobalt-base superalloys, Acta Mater. 77 (2014) 352–359.



- [17] M. S. Titus, Y. M. Eggeler, A. Suzuki, T. M. Pollock, Creep-induced planar defects in L12-containing Co- and CoNi-base single-crystal superalloys, *Acta Mater.* 3 (2014) 1–10.
- [18] B. H. Kear, J. M. Oblak, A. F. Giamei, Stacking faults in gamma prime Ni<sub>3</sub>(Al, Ti) precipitation hardened nickel-base alloys, *Metall. Trans. I* (1970) 2477–2486.
- [19] G. Leverant, B. Kear, The mechanism of creep in gamma prime precipitation-hardened nickel-base alloys at intermediate temperatures, *Metall. Mater. Trans. B* 1 (1970) 491–498.
- [20] N. Matan, D. Cox, P. Carter, M. Rist, C. Rae, R. Reed, Creep of CMSX-4 superalloy single crystals: effects of misorientation and temperature, *Acta Mater.* 47 (1999) 1549–1563.
- [21] C. M. F. Rae, R. C. Reed, Primary creep in single crystal superalloys: Origins, mechanisms and effects, *Acta Mater.* 55 (2007) 1067–1081.
- [22] G. Viswanathan, R. Shi, A. Genc, V. Vorontsov, L. Kovarik, C. Rae, M. Mills, Segregation at stacking faults within the  $\gamma'$  phase of two Ni-base superalloys following intermediate temperature creep, *Scr. Mater.* 94 (2015) 5–8.
- [23] A. J. Elliott, T. M. Pollock, Thermal Analysis of the Bridgman and Liquid-Metal-Cooled Directional Solidification Investment Casting Processes, *Metall. Mater. Trans. A* 38 (2007) 871–882.
- [24] J. D. Miller, T. M. Pollock, Development and Application of an Optimization Protocol for Directional Solidification: Integrating Fundamental Theory, Experimentation and Modeling Tools, in: E. S. Huron, R. C. Reed, M. C. Hardy, M. J. Mills, R. E. Montero, P. D. Portella, J. Telesman (Eds.), *Superalloys 2012*, TMS, 2012, pp. 653–662.
- [25] C. L. Brundidge, Development of a processing-structure-fatigue property model for single crystal superalloys (2011).
- [26] A. J. D’Alfonso, B. Freitag, D. Klenov, L. J. Allen, Atomic-resolution chemical mapping using energy-dispersive x-ray spectroscopy, *Phys. Rev. B* 81 (2010) 100101.
- [27] M.-W. Chu, S. C. Liou, C.-P. Chang, F.-S. Choa, C. H. Chen, Emergent Chemical Mapping at Atomic-Column Resolution by Energy-Dispersive X-Ray Spectroscopy in an Aberration-Corrected Electron Microscope, *Phys. Rev. Lett.* 104 (2010) 196101.
- [28] L. J. Allen, A. J. D’Alfonso, B. Freitag, D. O. Klenov, Chemical mapping at atomic resolution using energy-dispersive x-ray spectroscopy, *MRS Bull.* 37 (2012) 47–52.
- [29] J. Edington, *Practical Electron Microscopy in Materials Science*, TechBooks, 1976.
- [30] G. Thomas, M. J. Goringe, *Transmission Electron Microscopy of Materials*, John Wiley & Sons, Inc., 1979.
- [31] D. B. Williams, C. B. Carter, *Transmission Electron Microscopy: A Textbook for Materials Science*, 2nd ed., Springer, 2009.
- [32] B. H. Kear, A. F. Giamei, Slip and Climb Processes in gamma’ Precipitation Hardened Nickel-Base Alloys, *Scr. Metall.* 2 (1968) 287–293.
- [33] H. Suzuki, Chemical Interaction of Solute Atoms with Dislocations, in: 688th Rep. Res. Inst. Iron, Steel, other Met., 1952, pp. 455–463.
- [34] R. Herschitz, D. N. Seidman, Atomic resolution observations of solute-atom segregation effects and phase transitions in stacking faults in dilute cobalt alloys-I. Experimental results, *Acta Metall.* 33 (1985) 1547–1563.

- [35] G. Han, I. Jones, R. Smallman, Direct evidence for Suzuki segregation and Cottrell pinning in MP159 superalloy obtained by FEG(S)TEM/EDX, *Acta Mater.* 51 (2003) 2731–2742.
- [36] B. G. Mendis, Suzuki segregation in a binary Cu-Si alloy, *J. Electron Microsc.* (Tokyo). 53 (2004) 311–323.
- [37] Y. Koizumi, T. Nukaya, S. Suzuki, S. Kurosu, Y. Li, H. Matsumoto, K. Sato, Y. Tanaka, A. Chiba, Suzuki segregation in CoNi-based superalloy at 973K: An experimental and computational study by phase-field simulation, *Acta Mater.* 60 (2012) 2901–2915.
- [38] S. Y. Yang, M. Jiang, L. Wang, Thermodynamic Description of the  $\gamma'$  Phase in the Co-Al-W Based Superalloys, *Mater. Sci. Forum* 747-748 (2013) 654–658.
- [39] J. F. Nie, Y. M. Zhu, J. Z. Liu, X. Y. Fang, Periodic segregation of solute atoms in fully coherent twin boundaries., *Science* (80-. ). 340 (2013) 957–960.
- [40] P. Lechner, S. Eckbauer, R. Hartmann, S. Krisch, D. Hauff, R. Richter, H. Soltau, L. Strueder, C. Fiorini, E. Gatti, A. Longoni, M. Sampietro, Silicon drift detectors for high resolution room temperature X-ray spectroscopy, *Nucl. Instruments Methods Phys. Res. A* 377 (1996) 346–351.
- [41] V. Vorontsov, L. Kovarik, M. Mills, C. Rae, High-resolution electron microscopy of dislocation ribbons in a CMSX-4 superalloy single crystal, *Acta Mater.* 60 (2012) 4866–4878.
- [42] P. J. H. Denteneer, W. van Haeringen, Stacking-fault energies in semiconductors from first-principles calculations, *Journal of Physics C: Solid State Physics* 20 (1987) L883–L887.
- [43] A. Zunger, S.-H. Wei, L. G. Ferreira, J. E. Bernard, Special quasirandom structures, *Physical Review Letters* 65 (1990) 353–356.
- [44] A. Mottura, A. Janotti, T. M. Pollock, A first-principles study of the effect of Ta on the superlattice intrinsic stacking fault energy of L12-Co3(Al,W), *Intermetallics* 28 (2012) 138–143.
- [45] P. Hohenberg, W. Kohn, Inhomogeneous electron gas, *Physical Review B* 136 (1964) 864–871.
- [46] W. Kohn, L. J. Sham, Self-consistent equations including exchange and correlation effects, *Physical Review* 140 (1965) A1133–A1138.
- [47] G. Kresse, J. Furthmüller, Efficient iterative schemes for ab initio total-energy calculations using a plane-wave basis set, *Physical Review B* 54 (1996) 11169–11186.
- [48] J. Hafner, Materials simulations using VASP - a quantum perspective to materials science, *Computer Physics Communications* 177 (2007) 6–13.
- [49] D. J. C. MacKay, *Information Theory, Inference, and Learning Algorithms*, Cambridge University Press, 2003.
- [50] C. E. Rasmussen, *Gaussian Processes in Machine Learning*, *Advanced Lectures on Machine Learning* 3176 (2004) 63–71.
- [51] H. Suzuki, The Yield Strength of Binary Alloys, in: *Dislocations Mech. Prop. Cryst.*, 1957, pp. 361–390.
- [52] H. Suzuki, Segregation of Solute Atoms to Stacking Faults, *J. Phys. Soc. Japan* 17 (1962) 322–325.
- [53] J. P. Hirth, Thermodynamics of Stacking Faults, *Metall. Trans.* 1 (1970) 2367–2374.
- [54] M. Loubradou, J. M. Penisson, R. Bonnet, Structural ledges at precipitate / matrix interfaces in a (Ni, Co) superalloys: atomic structures and elastic fields, *Ultramicroscopy* 51 (1993) 270–281.

- [55] B. Cheong, Y. C. Feng, D. E. Laughlin, L12 to D019 Structural Ordering During the fcc to hcp Transformation in a CoCrTa Alloy, *Scr. Metall. Mater.* 30 (1994) 1419–1424.
- 735 [56] Q. Z. Chen, A. H. W. Ngan, B. J. Duggan, The L12 to D019 transformation in the intermetallic compound Fe<sub>3</sub>Ge, *J. Mater. Sci.* 33 (1998) 5405–5414.
- [57] P. A. Carvalho, P. M. Bronsveld, B. J. Kooi, J. T. M. D. Hosson, On the fcc D0 19 transformation in Co W alloys, *Acta Mater.* 50 (2002) 4511–4526.
- 740 [58] B. H. Kear, A. F. Giamei, G. R. Leverant, J. M. Oblak, On Intrinsic/Extrinsic Stacking Fault Pairs in the L12 Lattice, *Scr. Metall.* 3 (1969) 123–130.
- [59] B. H. Kear, A. F. Giamei, G. R. Leverant, J. M. Oblak, Stacking fault pairs in the L12 lattice, *Scr. Metall.* 3 (1969) 123–130.
- [60] J. P. Hirth, J. Lothe, *Theory of Dislocations*, 2nd ed., Krieger Publishing Company, 1992.
- 745 [61] A. H. Cottrell, M. A. Jaswon, Distribution of Solute Atoms Round a Slow Dislocation, *Proc. R. Soc. A Math. Phys. Eng. Sci.* 199 (1949) 104–114.
- [62] Y.-W. Cui, G. Xu, R. Kato, X.-G. Lu, R. Kainuma, K. Ishida, Interdiffusion and Atomic Mobility for Face-Centered Cubic (FCC) Co-W Alloys, *Metall. Mater. Trans. A* 44 (2013) 1621–1625.
- [63] R. Srinivasan, G. F. Eggeler, M. J. Mills,  $\gamma'$ -cutting as rate-controlling recovery process during high-temperature and low-stress creep of superalloy single crystals, *Acta Mater.* 48 (2000) 4867–4878.
- 750 [64] L. J. Carroll, Q. Feng, T. M. Pollock, Interfacial Dislocation Networks and Creep in Directional Coarsened Ru-Containing Nickel-Base Single-Crystal Superalloys, *Metall. Mater. Trans. A* 39 (2008) 1290–1307.
- [65] D. A. Porter, K. E. Easterling, *Phase Transformations in Metals and Alloy*, 2nd ed., Chapman & Hall, 1993.
- 755 [66] H. Frost, M. Ashby, *Deformation-Mechanism Maps, The Plasticity and Creep of Metals and Ceramics*, Pergamon Press, 1982.
- [67] G. R. Leverant, B. H. Kear, J. M. Oblak, Creep of precipitation-hardened nickel-base alloy single crystals at high temperatures, *Metall. Trans.* 4 (1973) 355–362.
- 760 [68] T. M. Pollock, A. S. Argon, Creep resistance of CMSX-3 nickel base superalloy single crystals, *Acta Metall. Mater.* (1992) 1–30.
- [69] T. Gabb, S. Draper, D. Hull, R. Mackay, M. Nathal, The role of interfacial dislocation networks in high temperature creep of superalloys, *Mater. Sci. Eng. A* A118 (1989) 59–69.
- 765 [70] T. M. Pollock, R. D. Field, Dislocations and High-Temperature Plastic Deformation of Superalloy Single Crystals, in: F. R. N. Nabarro, M. S. Duesbery (Eds.), *Dislocations in Solids*, Elsevier Science B.V., 2002, pp. 549–614.
- [71] S. Neumeier, C. Zenk, H. Rehman, M. Göken, The Effect of Rhenium in Co-base Superalloys A Comparison with Ni-base Superalloys, in: *TMS 2014*, 2014.
- [72] N. L. Okamoto, T. Ohashi, H. Adachi, K. Kishida, H. Inui, P. Veyssi re, Plastic deformation of polycrystals of Co<sub>3</sub>(Al,W) with the L12 structure, *Philos. Mag.* 91 (2011) 3667–3684.
- 770 [73] A. Mottura, A. Janotti, T. M. Pollock, Alloying Effects in the gamma' Phase of Co-based Superalloys, in: *Superalloys 2012*, 2012, pp. 685–693.

- [74] J. L. Murray, The Co-Ti (Cobalt-Titanium) System, *Bull. Alloy Phase Diagrams* 3 (1982) 74–85.
- [75] S. Kobayashi, Y. Tsukamoto, T. Takasugi, Phase equilibria in the Co-rich Co-Al-W-Ti quaternary system, *Intermetallics* 19 (2011) 1908–1912.
- 775 [76] L. Zhou, C. Wang, Y. Yu, X. Liu, H. Chinen, T. Omori, I. Ohnuma, R. Kainuma, K. Ishida, Experimental investigation and thermodynamic calculation of the phase equilibria in the CoNbTa ternary system, *J. Alloys Compd.* 509 (2011) 1554–1562.
- [77] K. Lu, L. Lu, S. Suresh, Strengthening Materials by Engineering Coherent Internal Boundaries at the Nanoscale, *Science* (80-. ). 324 (2009) 349–352.
- 780 [78] K. Momma, F. Izumi, VESTA 3 for three-dimensional visualization of crystal, volumetric and morphology data, *J. Appl. Crystallogr.* 44 (2011) 1272–1276.
- [79] J. Zhu, M. S. Titus, T. M. Pollock, Experimental Investigation and Thermodynamic Modeling of the Co-Rich Region in the Co-Al-Ni-W Quaternary System, *J. Phase Equilibria Diffus.* (2014).

## 8. Tables

Table 1: Compositions (at.%) and heat treatment schedules of Co-base alloys investigated.

Alloy	Co	Ni	Al	W	Ta	Cr	Ti	Solution	Age
2Ta	79.4	-	8.8	9.8	2.0	-	-	1250°C/12hrs	1000°C/100hrs
CrTa	78.4	-	7.8	7.8	1.5	4.5	-	1300°C/6hrs	900°C/150hrs
6Ti	79.0	-	6.7	8.1	-	-	6.2	1225°C/60hrs	1000°C/100hrs
CoNi-C	38.0	38.0	9.3	6.9	1.4	6.4	-	1230°C/12hrs	950°C/100hrs

Table 2: Creep conditions of investigated alloys

Alloy	Creep Temp (°C)	Stress (MPa)	Strain (%)	Hours to Interruption	$\dot{\epsilon}_{min}(\times 10^{-8}s^{-1})$
2Ta-1	900	345	0.6	89	0.7
2Ta-2	900	345	2.0	190	0.7
CrTa	900	310	2.2	65	1.4
6Ti	900	310	2.3	356	0.5
CoNi-C	900	275	2.1	117	1.0

Table 3: Relevant phase crystallography. SBS = Strukturbericht symbol, PS = Pearson Symbol, SG = Space Group.

SBS	PS	Phase	Prototype	SG#	SG
A1	cF4	$\gamma$ -(Co)	Cu	225	Fm $\bar{3}$ m
L1 <sub>2</sub>	cP4	$\gamma'$ -Co <sub>3</sub> (Al,W)	Cu <sub>3</sub> Au	221	Pm $\bar{3}$ m
D0 <sub>19</sub>	hP8	(SISF)	Ni <sub>3</sub> Sn	194	P6 <sub>3</sub> /mmc
D0 <sub>24</sub>	hP16	(SESF)	Ni <sub>3</sub> Ti	194	P6 <sub>3</sub> /mmc
A3	hP2	$\epsilon$ -(Co)	Mg	194	P6 <sub>3</sub> /mmc

Table 4: SISF chemical fluctuation trends for all alloying elements in the Co- and CoNi-base alloys investigated.

Alloy	Enhancement	Depletion	No Change
2Ta	Ta,W	Co,Al	
CrTa	Ta,W	Co,Al,Cr	
6Ti	W	Co,Al	Ti
CoNi-C	Co,W,Cr,Ta	Ni,Al	



Figure 1: Conventional TEM micrographs of the 2Ta alloy crept to 0.6% in (a), 2.0% in (b) and (c). The foil normals are  $[001]$  for (a) and (b), and  $[011]$  for (c). In all cases, a  $\mathbf{g} = (200)$  reflection is used, as shown by the arrows. A selected area diffraction pattern is shown in the upper right corner in all figures. The precipitates appear black in (b) due to numerous overlapping faults in the  $\beta$  phase, and thin black lines, which are SISFs in near edge-on configuration, are observed stretching across the precipitates in (c).

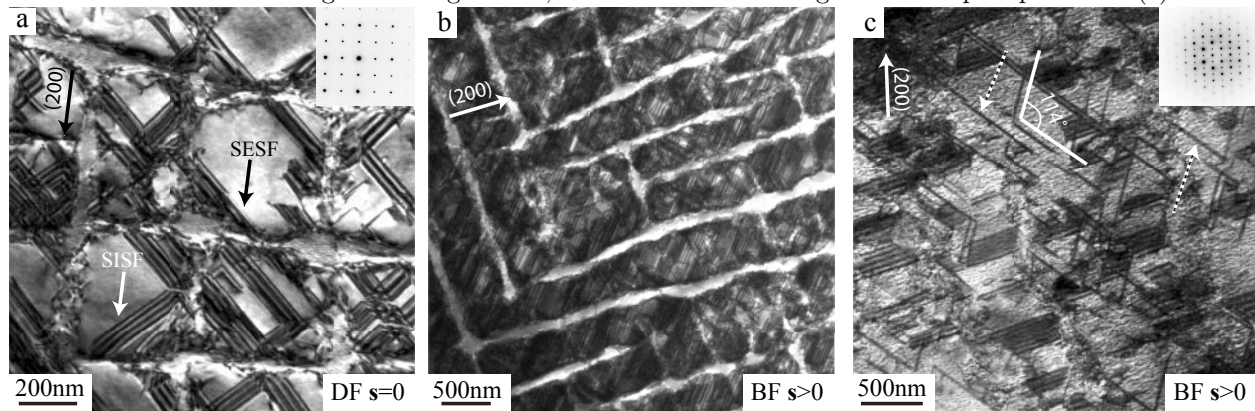




Figure 2: High resolution HAADF STEM images for a SISF and SESF in the 2Ta alloy are shown in (a) and (d) with their respective Fourier transforms shown in the lower right. The stacking sequence along the  $111$  planes changes from ABCABC outside of the stacking faults to  $D0_{19}$  and  $D0_{24}$  stacking inside the SISF and SESF, respectively. The  $111$  planes are labeled A (red), B (yellow), C (green) in (a) and (d), and the corresponding structures are shown schematically in (b) and (e) [78]. Vertically-integrated line profiles are shown in (c) and (f) for the SISF and SESF, respectively. Enhanced intensity is observed inside of the faults.

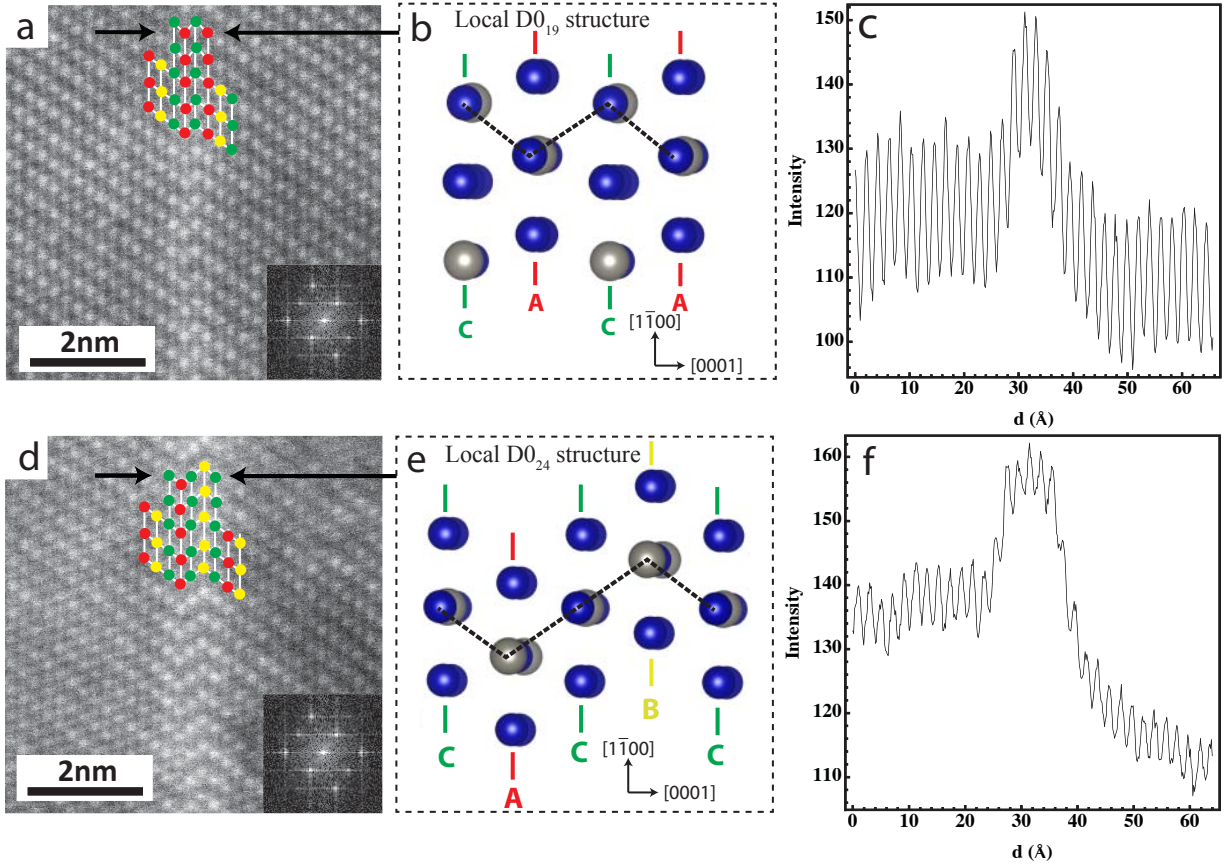


Figure 3: A high resolution HAADF STEM image is shown in (a) and the corresponding EDS maps for Co, Al, W, and Ta are shown in (b-e). The EDS maps were binned by  $4\times 4$  in order to enhance reproduction quality. Faint contrast changes corresponding to changes in composition are observed near the SISF for each element.

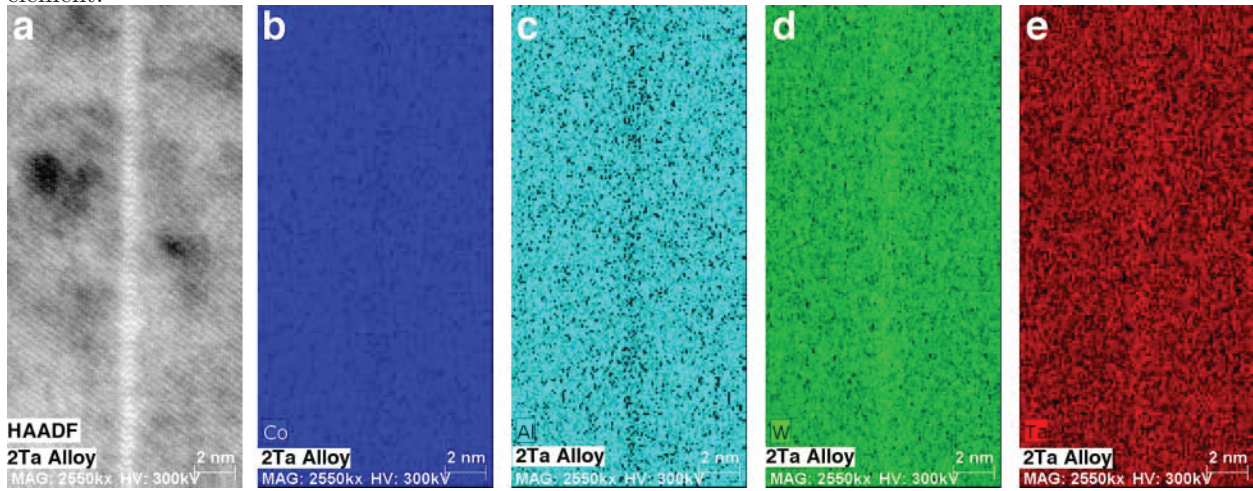


Figure 4: Vertically-integrated line scans are shown for the 2Ta, CrTa, 6Ti, and CoNi-C alloys in. The line scans were quantified using standard k-factors, and the results are shown in percent change from average  $\gamma'$  concentration. Each line crossing the ordinate represents a 30% change in composition, and the individual elements are offset from each other by 30% for clarity. In the Co-base alloys (2Ta, CrTa, and 6Ti alloys), Co, Al, and Cr depleted from the fault, and W and Ta always segregated to the fault. Titanium did not exhibit any segregation behavior at the fault. In the CoNi-C alloy, Ni was observed to deplete from the fault, and Co was enhanced.

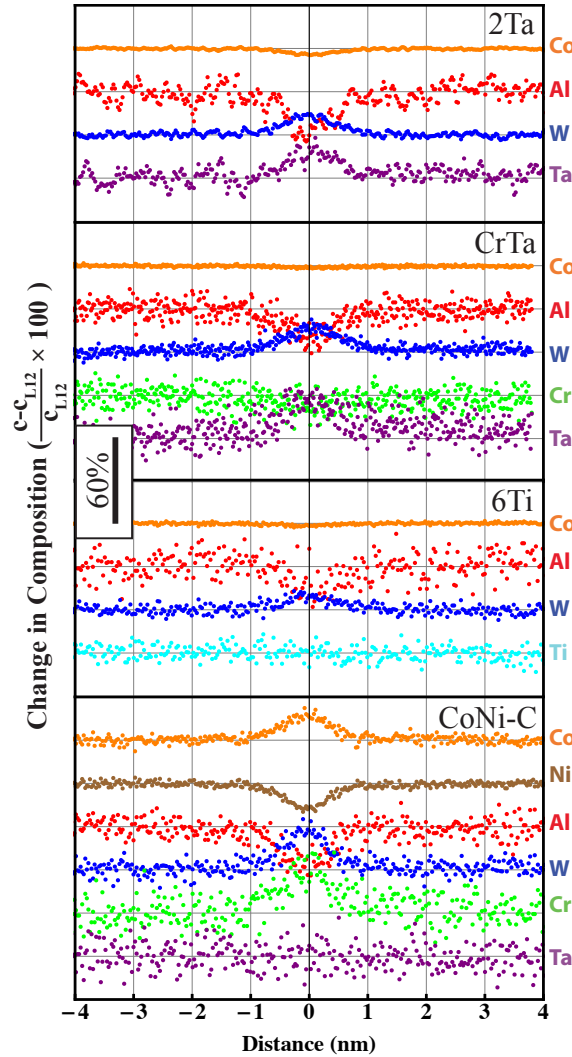


Figure 5: Partial Co-Al-W ternary phase diagram calculated at 900°C from Ref. [79]. The phases present in the diagram include  $\gamma$  (A1),  $\gamma'$  (L1<sub>2</sub>),  $\beta$  (B2), Co<sub>3</sub>W (D0<sub>19</sub>), and  $\mu$  (D8<sub>5</sub>). The dashed light red line along 75at.% Co ranges from Co<sub>3</sub>Al to Co<sub>3</sub>W. The red arrow represents the direction of compositional change for faults in Co-base alloys. The change in composition from the  $\gamma'$  phase field to the Co<sub>3</sub>W phase field includes an increase in Co and W, and a decrease in Al.

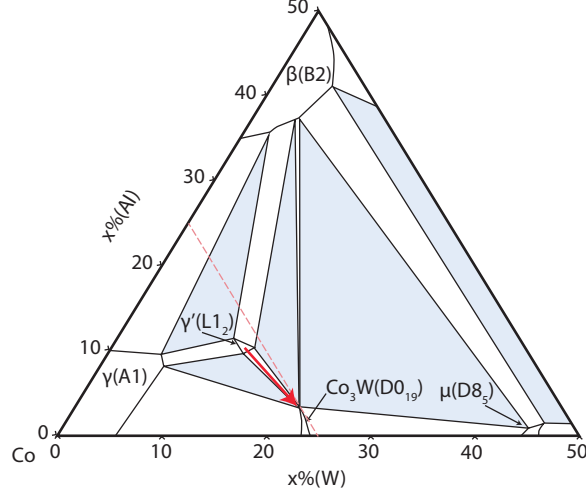


Figure 6: Sixteen compositions were used to determine the SISF energy as a function of composition, as shown in (a). The SISF energy in the pseudo-ternary Co<sub>3</sub>Al-Co<sub>3</sub>W-Co<sub>3</sub>Ta system is shown in (b). A contour line at 0 mJ/m<sup>2</sup> is drawn for clarity. Negative SISF energies correspond to a stabilization of the D0<sub>19</sub> phase.

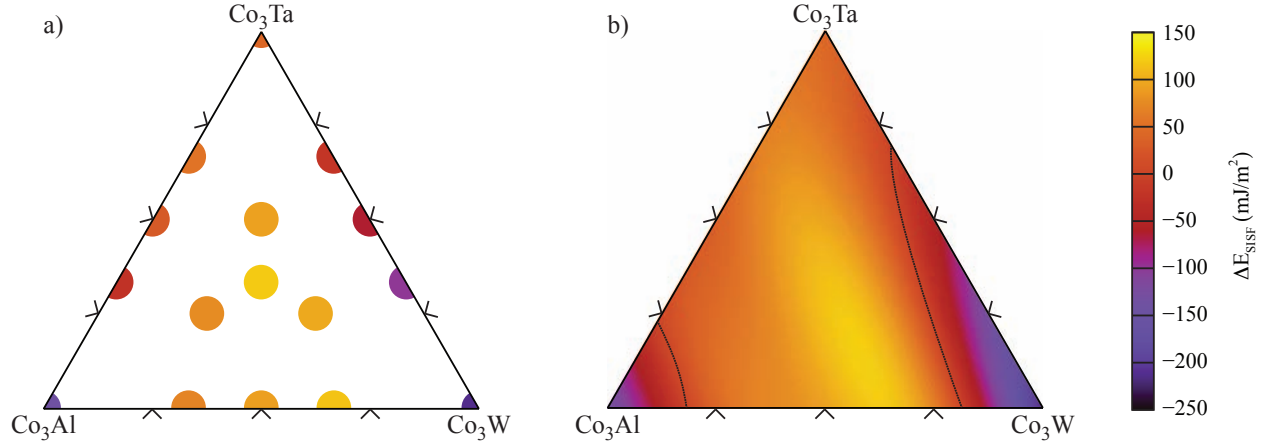


Figure 7: Schematic of a SISF shearing process that involves  $\frac{1}{3}\langle 112 \rangle$  and  $\frac{1}{6}\langle 112 \rangle$  Shockley superpartial dislocations, blue and red, respectively in (a-c). The two superpartials are separated in their equilibrium configuration in (a) by a segregated SISF, denoted by the series of “XX”. A virtual displacement is made on the leading partial of length  $\delta r$  in (b), and a small region of unsegregated SISF is then formed. At a critical resolved shear stress, the leading partial will escape, as shown in (c). The resolved shear stress vs. separation distance is shown schematically in (d) for two different segregated SISF energies, such that  $\gamma_{s1} > \gamma_{s2}$ . If segregation is allowed during the shearing process, the relevant breakaway stresses change, as shown in (e) where the dotted black lines represent the breakaway stresses for unsegregated SISFs.

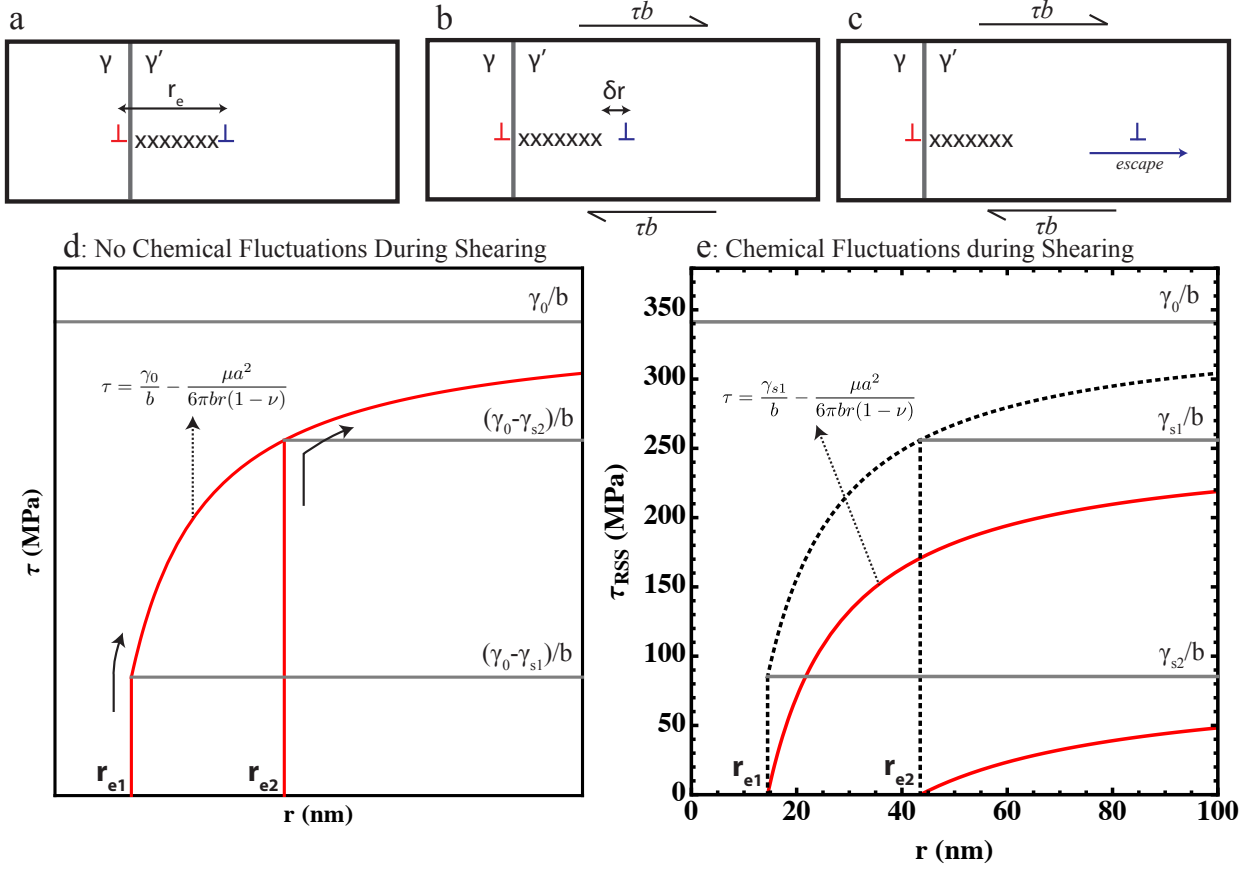
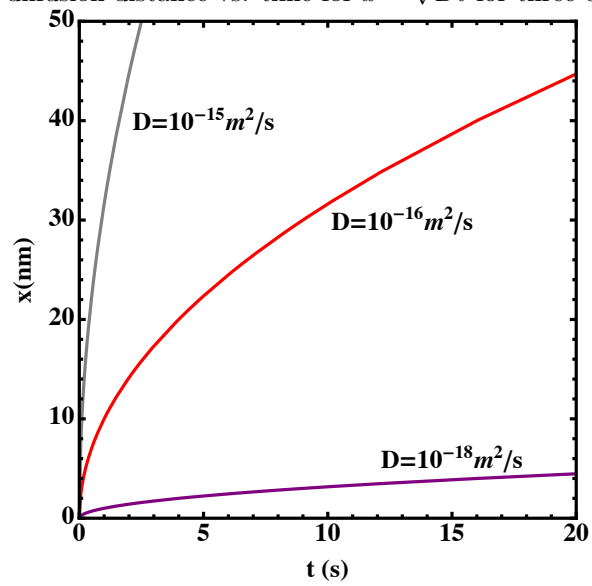


Figure 8: Graph of diffusion distance vs. time for  $x = \sqrt{Dt}$  for three diffusion coefficients.



## Appendix A. First-principles Calculations

All density functional theory [1, 2] calculations were performed using the Vienna Ab-initio Simulation Package (VASP) [3, 4]. The electron-ion interactions were described using the projector augmented wave (PAW) method [5, 6], while the spin-polarized generalised gradient approximation (GGA) parameterised by Perdew et al [7] was used to approximate the exchange and correlation functional. Plane waves were included up to 360 eV, which was deemed sufficient for accurate convergence. All geometric relaxations were carried out by evaluating the projector operators in real space, and an additional iteration of the electronic self-consistent cycle was performed evaluating the projector operators in reciprocal space to ensure high accuracy. The Monkhorst-Pack scheme was used to define the k-point mesh, with a density higher than  $5 \times 10^5$  k-points/ $\text{\AA}^{-3}$  [8] and a Methfessel-Paxton smearing with a sigma of 0.1 eV was used [9]. The electronic self-consistent cycles were interrupted once the forces acting on all the ions fell below  $10^{-3}$  eV/ $\text{\AA}$ .

The special quasi-random structures [10] for the  $\text{Li}_2$  and  $\text{D}_{0.19}$  crystal structures were obtained using the Alloy Theoretic Automated Toolkit (ATAT) [11–14]. Computational requirements limited the search of  $\text{A}_3(\text{B}_{0.5}\text{C}_{0.5})$  and  $\text{A}_3(\text{B}_{0.25}\text{C}_{0.25}\text{D}_{0.5})$  SQSs to 32-atom supercells, while  $\text{A}_3(\text{B}_{0.33}\text{C}_{0.66})$  and  $\text{A}_3(\text{B}_{0.33}\text{C}_{0.33}\text{D}_{0.33})$  SQS were sought amongst 24-atom supercells. The SQSs used for the  $\text{A}_3(\text{B}_{0.5}\text{C}_{0.5})$  chemical composition are the same as those used by Mottura et al in earlier work [15] and match the pair correlation functions of an ideal random distribution up to 6<sup>th</sup> neighbours. The SQSs for the  $\text{A}_3(\text{B}_{0.33}\text{C}_{0.33}\text{D}_{0.33})$  composition also match the pair correlation functions of an ideal random distribution up to 6<sup>th</sup> neighbours. The SQSs for the  $\text{A}_3(\text{B}_{0.33}\text{C}_{0.66})$  composition match the pair correlation functions of an ideal random distribution up to 4<sup>th</sup> neighbours, while the SQSs for the  $\text{A}_3(\text{B}_{0.25}\text{C}_{0.25}\text{D}_{0.5})$  composition match the pair correlation functions of an ideal random distribution up to 2<sup>nd</sup> neighbours.

## Appendix References

- [1] P. Hohenberg, W. Kohn, Inhomogeneous electron gas, *Physical Review B* 136 (1964) 864–871.
- [2] W. Kohn, L. J. Sham, Self-consistent equations including exchange and correlation effects, *Physical Review* 140 (1965) A1133–A1138.
- [3] G. Kresse, J. Furthmuller, Efficient iterative schemes for ab initio total-energy calculations using a plane-wave basis set, *Physical Review B* 54 (1996) 11169–11186.

- [4] J. Hafner, Materials simulations using VASP - a quantum perspective to materials science, *Computer Physics Communications* 177 (2007) 6–13.
- [5] P. E. Blöchl, Projector augmented-wave method, *Physical Review B* 50 (1994) 17953–17979.
- 820 [6] G. Kresse, D. Joubert, From ultrasoft pseudopotentials to the projector augmented-wave method, *Physical Review B* 59 (1999) 1758–1775.
- [7] J. P. Perdew, K. Burke, M. Ernzerhof, Generalized gradient approximation made simple, *Physical Review Letters* 77 (1996) 3865–3868.
- 825 [8] H. J. Monkhorst, J. D. Pack, Special points for Brillouin-zone integrations, *Physical Review B* 13 (1976) 5188–5192.
- [9] M. Methfessel, A. T. Paxton, High-precision sampling for Brillouin-zone integration in metals, *Physical Review B* 40 (1989) 3616–3621.
- [10] A. Zunger, S.-H. Wei, L. G. Ferreira, J. E. Bernard, Special quasirandom structures, *Physical Review Letters* 65 (1990) 353–356.
- 830 [11] A. van de Walle, M. Asta, G. Ceder, The alloy theoretic automated toolkit: A user guide, *CALPHAD* 26 (2002) 539–553.
- [12] A. van de Walle, G. Ceder, Automating First-Principles Phase Diagram Calculations, *Journal of Phase Equilibria* 23 (2002) 348–359.
- 835 [13] A. van de Walle, Multicomponent multisublattice alloys, nonconfigurational entropy and other additions to the Alloy Theoretic Automated Toolkit, *CALPHAD* 33 (2009) 266–278.
- [14] G. L. W. Hart, R. W. Forcade, Algorithm for generating derivative structures, *Physical Review B* 77 (2008) 224115.
- [15] A. Mottura, A. Janotti, T. M. Pollock, A first-principles study of the effect of Ta on the superlattice intrinsic stacking fault energy of  $\text{Li}_2\text{-Co}_3(\text{Al,W})$ , *Intermetallics* 28 (2012) 138–143.